This is a preprint, the final version is subject to change, of the American Mineralogist (MSA)
Cite as Authors (Year) Title. American Mineralogist, in press.
(DOI will not work until issue is live.) DOI: http://dx.doi.org/10.2138/am-2017-5805

Iron L_3-edge spectroscopic evaluation of iron oxide and oxy-hydroxide coordination

Revision 1

Bjorn P. von der Heyden[a,*], Alakendra N. Roychoudhury[a], Tolek Tyliszczak[c], Satish C. B. Myneni[b]

a. Department of Earth Sciences, Stellenbosch University, Private Bag X1, Matieland, 7602, South Africa
b. Department of Geosciences, Princeton University, Princeton, NJ 08544, USA.
c. Advanced Light Source, Lawrence Berkeley National Laboratory, University of California, Berkeley, CA 94720, USA.

* Corresponding author. Email: bvon@sun.ac.za
Phone: +27 21 808 3122

ABSTRACT

The iron (Fe) $L_{2,3}$-edge X-ray Absorption Near-Edge Structure (XANES) spectrum is sensitive to the local coordination environment around the Fe metal centre, making it a useful probe for understanding Fe mineral speciation. The two dominant spectral peaks in the Fe L_3-edge are parameterised according to the difference in the energy position (ΔeV), and the quotient (intensity ratio) of the two peaks' maxima. Variations in the ΔeV value are strongly linked to factors that impact on the strength of the ligand field (e.g., Fe valence state, coordination number, and the nature of ligand bonding). The intensity ratio is affected by the strength of the ligand field and by the composition of the resultant molecular orbitals. The Fe valence state also strongly affects the intensity ratio, and an intensity ratio equal to one can be used to distinguish between Fe(II) and Fe(III) minerals.

The effects of polyhedral distortion on the magnitudes of ΔeV and intensity ratio values were tested by considering the Fe oxide and –oxy-hydroxide mineral system, in which ligand effects are limited to the differences between the oxygen and hydroxyl ligands. In this system, the distribution of Fe oxide and –oxy-hydroxide minerals on a ΔeV versus intensity ratio two-parameter plot could be explained by considering the Fe valence state, the ligand chemistry and the site symmetry of the Fe polyhedra. Furthermore, the ΔeV and intensity ratio values were found to be anti-correlated with respect to the various distortion measures considered in this study (e.g., polyhedral volume distortion percentage). This two-parameter plot is thus presented as a standard-less phase-specific identification tool for use in Fe speciation studies, applicable to both natural systems (e.g., aerosols, aquatic colloids) as well as to engineered systems (e.g., nanoparticle synthesis). A major advantage of this technique is that it is applicable to both crystalline and poorly crystalline phases, thus enhancing our ability to study amorphous and nano-crystalline phases that are typically difficult to characterise using X-ray diffraction techniques.

Keywords: Fe; iron; L-edge; XANES; iron oxide; iron oxy-hydroxide; ferrihydrite

INTRODUCTION

Iron $L_{2,3}$-edge X-ray absorption spectroscopy (XAS) provides important electronic information about the local atomic structure around the Fe centre and this technique has thus been utilized in a considerable number of studies; ranging from biogeochemistry (Wang et al., 1995; Calvert et al., 2005; Benzerara et al., 2007; Chan et al., 2009; Miot et al., 2009) and mineralogy (van Aken et al., 1998; Miyajima et al., 2004), to materials chemistry (Labatut et al., 1998; Grandjean et al., 1999; Mikhlin et al., 2005; Augustsson et al., 2005; Chen et al., 2007; Shirakawa et al., 2007). Much of this work, especially in hydrated systems, is possible because of the advancements in soft X-ray instrumentation (Cramer et al., 1992; Padmore and Warwick, 1994) and because of the volumes of early vacuum-based work devoted to developing a fundamental understanding of the L-edge spectral features (van der Laan and Kirkman, 1992; Cressey et al., 1993; Crocombette et al., 1995; de Groot, 2005). The Fe L-edge represents the probability and occurrence of dipole-allowed electronic transitions from the *2p* ground state to *3d*-like molecular orbitals, and variations in the resultant spectra are interpreted as a function of valence state, site occupation, symmetry, spin state and degree of distortion (van der Laan and Kirkman, 1992; Schofield et al., 1995; de Groot, 2005; Miedema and de Groot, 2013). The chemical information contained in the Fe L-edge complements the information obtained from Fe K-edge analyses; and the L-edge technique has been chosen for use in this study because of its better resolution of fine structure, higher absorption cross section (important in spectro-microscopy), and lower intrinsic life-time broadening (e.g., de Groot, 2005).

67

68 The *2s* and *2p* electronic transitions of Fe L-edge can be probed either by using XAS
69 techniques at a synchrotron light source, or by Electron Energy-Loss Spectroscopy
70 (EELS) using a transmission electron microscope (TEM). A comprehensive evaluation of
71 these two techniques suggests that XAS is superior over EELS particularly when
72 environmentally relevant hydrated samples are considered (e.g. Dynes et al., 2006;
73 Bluhm et al., 2006). The foremost reason for this is that XAS allows for the molecular
74 level investigation of samples in their pristine state, without the need for sample drying,
75 which can alter the chemical state of the elements of interest and can induce shrinkage,
76 aggregation and water loss from the chemically-important hydration shells. In addition,
77 the spectral resolution that can be achieved using XAS is superior to the spectral
78 resolution associated with EELS techniques.

79

80 Application of the Fe $L_{2,3}$-edge XAS for speciation and mineralogical studies, especially
81 in samples of environmental significance, have thus far largely been limited to valence
82 state quantification studies (Cressey et al., 1993; van Aken et al., 2002; Miyajima et al.,
83 2004; Calvert et al., 2005; Cavé et al., 2006; Dynes et al., 2006; Bourdelle et al., 2013).
84 Fe oxidation state is undoubtedly a fundamental parameter governing the Fe behaviour in
85 biogeochemical systems, as well as the Fe properties in material science and engineering
86 applications. However, given that the Fe L-edge probes local electronic structure (van der
87 Laan and Kirkman, 1992; Cressey et al., 1993); the resultant spectrum is also sensitive to
88 variations in coordination and ligand bonding. Although a recent study has made use of
89 fine differences in the Fe L_3-edge XAS to investigate ferrihydrite structure (Peak and

Regier, 2012), to our knowledge, there has not as yet been a systematic experimental study investigating the changes in XAS spectral features in response to varying Fe speciation. A number of studies have used the Fe L-edge as a speciation probe for investigating Fe phases, primarily the Fe-oxidation state, in environmental samples. Chan et al. (2004) use Fe L-edge Scanning Transmission X-ray Microscopy (STXM) mapping and Fe L-edge X-ray photoelectron emission spectromicroscopy to infer that mineralised bio-filaments consist of amorphous Fe oxy-hydroxide. Interactions with biology have further been investigated by Miot and co-workers (2009), who used the Fe L-edge XAS to measure the rates and the extent of Fe oxidation by bacteria; and Liu et al. (2015) who confirm pyrite transformation to Fe(III) phases during bioleaching. Other studies have utilised the Fe L-edge to understand and characterise the mineral-organic associations in soils (Chen and Sparks, 2015) and marine particles (von der Heyden et al., 2014) and the Fe L-edge XAS has also been used to conclude that the observed Fe(II) in hydrothermal systems is not present as finely dispersed Fe(II) minerals, but rather that the Fe(II) is stabilized by complexation with particulate organic matter (Toner et al., 2009).

In this study, we synthesise high-purity Fe mineral standards which we analyse using high resolution Fe $L_{2,3}$-edge experimental XANES in order to extract detailed chemical information from their spectral features. These data are further compared to an extensive compilation of Fe L-edge XANES spectra published in the literature (von der Heyden et al., 2012 (supplementary material)). In particular, we parameterise the L_3-edge peak splitting (ΔeV) and the intensity (peak height) ratio associated with these split peaks (Fig. 1a), and use these parameters to explore the changes in Fe coordination environment as a

function of Fe mineral structure and chemistry. Although additional information can be derived from the Fe L-edge, this parameterisation approach benefits from its ease of use, consistency in peak identification and quantification, and a lack of a need for mineral standards for energy calibration. The L_3-edge peak-splitting can largely be attributed to the ligand field splitting of Fe d-orbitals into t_{2g} and e_g subsets, which are further divisible into molecular orbitals formed by ligand coordination (Todd et al., 2003a; de Groot, 2005). The ΔeV value is thus strongly linked to the energy levels of these molecular orbitals, whereas the intensity ratio value is also affected by the respective orbital compositions- with selection rules governing the likelihood of electronic transitions. By interpreting high-resolution L_3-edge XANES (X-ray Absorption Near-Edge Structure) spectra, this study investigates the factors that influence the ΔeV and intensity ratio values of the Fe L_3-edge for the polymorphs of the Fe oxide and oxy-hydroxide system. Fe mineral phases, particularly Fe oxides and –oxy-hydroxides, play an integral role in soil and sediment biogeochemical reactions (Cornell and Schwertmann, 2003) and in contaminant transformation and transport processes (Appelo and Postma, 2004; Hochella et al., 2005; von der Heyden and Roychoudhury, 2015), and are often small and difficult to differentiate in environmental samples by using traditional methods. The advantages of the Fe L-edge X-ray spectro-microscopic technique is that it has a spatial resolution of down to 10 nm and that it is able to evaluate the chemical and structural properties of both amorphous and crystalline phases. It is thus an ideal tool for examining the properties of sub- micrometer sized environmental samples- such as aquatic colloids (Lead and Wilkinson, 2006; Wiggington et al., 2007; von der Heyden, 2012, 2014) and aerosols (Krueger et al., 2004; Majestic et al., 2007, Takahama et al., 2008).

EXPERIMENTAL DETAILS

Synthesis of standards: Fe oxide and Fe (oxy-) hydroxide mineral standards (goethite (α-FeOOH), akaganeite (β-FeOOH), lepidocrocite (γ-FeOOH), hematite (α-Fe_2O_3), maghemite (γ-Fe_2O_3), magnetite (Fe_3O_4) and amorphous iron oxy-hydroxide) were prepared following the methods outlined in Schwertmann and Cornell (2000). The purities of the prepared standards were confirmed by X-ray diffraction (Rigaku XRD) and infrared spectroscopy (Bruker IFS 66v/s).

X-ray data collection: The scanning transmission X-ray microscopy (STXM) studies were conducted at the Molecular Environmental Sciences (MES) beamline 11.0.2 at the Advanced Light Source, Lawrence Berkeley National Laboratory, USA (see Bluhm et al., 2006). A few μL of the mineral suspension was placed on a 100 nm thick Si_3N_4 sample window and allowed to air-dry before being placed in the end-station for X-ray analysis. All X-ray scans were conducted in transmission mode in a 1 atm He environment and at ambient temperature. The end-station specifications; a 17 nm zone plate, a 1200 l/mm grating and 25 μm exit slits ensured theoretical spatial and spectral resolutions of 12 nm and 0.2 eV respectively. Energy calibration was achieved by setting the peak for neon *1s→3p* transitions to 867.3 eV.

159 **XANES spectral analysis:** Spectral stacks, representing image sequences taken at
160 incremental energy levels between 695 eV and 730 eV, were collected of the respective
161 Fe oxide and –oxy-hydroxide samples. Energy step-sizes between successive images
162 were 0.5 eV for the regions below and above the L_3-edge and 0.2 eV at the L_3-edge
163 region (705 -715 eV). Image stacks were overlain using Zimba code in the software
164 Axis2000 (Hitchcock, 2008) by implementing Sobel edge-enhancement and ensuring that
165 the images were accurately aligned. Thereafter, particle-free areas of the map were
166 chosen as the I_o, representing a background denominator; and between 60 and 90
167 individual particles per Fe oxide/-oxy-hydroxide were identified and analysed for their
168 averaged XANES spectra (except magnetite, observations from one spectrum).
169 Background correction was achieved by applying a one degree polynomial fit (WinXAS
170 software (Ressler, 1998)) to ensure that the pre-edge region (~695 – 702 eV) was parallel
171 to the x-axis and equal to zero, and that the post-edge region (>730 eV) was also parallel
172 to the x-axis. The effects of applying poorly-fitted background on the magnitudes of the
173 ΔeV and intensity ratio spectral parameters were tested, and found to be negligible
174 relative to the real spectral differences caused by differences in Fe mineralogy. Because
175 transmission X-ray spectrometry is sensitive to saturation effects, only the normalised
176 spectra with a maximum peak intensity (i.e., ~709.8 eV peak) in the range of 0.17 to 0.83
177 were interrogated further in this study (maghemite- 57 spectra; hematite- 48 spectra;
178 akaganeite- 66 spectra; goethite- 42 spectra; lepidocrocite- 32 spectra; and amorphous Fe
179 oxy-hydroxide- 53 spectra). This intensity range matched the intensity range that we have
180 observed in natural samples (von der Heyden et al., 2012, 2014); and limits X-ray
181 saturation effects from thicker particles. The effects of X-ray saturation were tested on

182 our subset of spectra and found to be negligible relative to the real spectral differences
183 caused by Fe mineralogy. The high energy peak intensity range (0.17 – 0.83) utilised in
184 this study further excluded thinner particles which are associated with weak spectra and
185 noise interference, and the collected spectra did thus not require mathematical smoothing.
186
187 The spectral parameters (ΔeV and intensity ratio) were calculated from the background-
188 subtracted spectra using the 'Search Min-Max' function in WinXAS (Ressler, 1998). This
189 approach, based on evaluating the first derivative of the spectra, excludes the possibility
190 for human-induced bias when evaluating the spectra and ensures consistency across the
191 299 standard Fe oxide and –oxy-hydroxide spectra considered in this study. The 'Search
192 Min-Max' function returns the energy position and the maximum peak absorbance
193 intensity data for all peaks contained within the Fe L-edge spectra. The ΔeV value was
194 calculated by subtracting the energy position of the low energy peak in the L_3-edge
195 (~708.2 eV) from the energy position of the high energy peak in the L_3-edge (~709.8 eV).
196 Similarly the intensity ratio of the split peaks in the Fe L_3-edge was calculated as the
197 quotient (or peak ratio) of the low energy peak's maximum absorbance intensity and the
198 high energy peak's maximum absorbance intensity (Fig. 1). The nature of these
199 operations ensures that the X-ray spectra do not require energy calibration and that the
200 ΔeV versus intensity ratio tool thus represents a standard-less method for characterising
201 Fe mineralogy. Spectral information for additional Fe-rich phases was compiled from
202 published literature. Peak height and energy data were obtained either by contacting the
203 corresponding author directly or by digitizing the published figures.
204

205 **Theoretical XANES calculations:** The charge-transfer multiplet program CTM4XAS
206 (Stravitski and de Groot, 2010) was used to further validate the experimental observations
207 made using Fe L-edge XANES spectroscopy. Theoretical spectral calculations can
208 accurately reproduce the observed splitting of the Fe L_3-edge (e.g., by stipulating in
209 CTM4XAS that 10Dq = 1.45, Slater integrals = 0.7 (after Miedema and de Groot, 2013)).
210 However, certain software limitations (e.g., complexity in modelling covalency
211 associated with bonding to oxygen and hydroxyl ligands (Miedema and de Groot, 2013),
212 the limited number of symmetry options available, and the sheer number of variables that
213 can impact on ΔeV and intensity ratio values (Fig. 2) complicate the accurate calculation
214 of the subtle, observed variations in the ΔeV and intensity ratio values when applied to
215 the Fe oxide and –oxy-hydroxide system. Accurate calculation of spectra is further
216 complicated by the presence of more than one Fe coordination site in some minerals (e.g.,
217 maghemite is characterised by Fe in tetrahedral and octahedral coordination).
218
219 **Local structure evaluations:** Additional comparisons were made between our spectral
220 dataset and various physical parameters of the respective Fe-oxide and –oxy-hydroxide
221 coordination polyhedra. Structural details for the different Fe phases were obtained from
222 the published crystal structure data (akaganeite (Post and Buchwald, 1991), ferrihydrite
223 (Michel et al., 2007), goethite (Gualtieri et al., 1999), hematite (Blake et al., 1966),
224 lepidocrocite (Wyckoff, 1963), maghemite (Shmakov et al., 1995), and magnetite (Fleet,
225 1986)). The investigations into their coordination environments were conducted using the
226 crystallographic programs IVTON (Balic-Zunic and Vickovic, 1996) and XSeed
227 (Atwood and Barbour, 2003).

RESULTS AND DISCUSSION

1. Theoretical influences of Fe L-edge spectral parameters

Although the L_3- and L_2-edges contain the same chemical information; the L_3-edge, representing the dipole-allowed $2p_{3/2}$ electronic transitions to the valence orbitals, shows sharper and better resolved spectral features than the corresponding L_2-edge. The splitting in the L_3-edge peak is largely due to the crystal field interaction; however, the spectral shape of the L_3-edge can also be influenced by inter-electronic repulsions, spin-orbit coupling, electrostatic multiplet effects, orbital covalency and core-hole effects (de Groot et al., 1990; Hocking et al., 2010; Miedema and de Groot, 2013). The split peaks of the L_3-edge can be parameterized by their peak intensity ratio value and a ΔeV value, representing the energy difference between the two peak positions (Fig. 1). Here we investigate the structural factors and bonding interactions that influence the ΔeV and intensity ratio values, thus determining the effects of mineralogical speciation on L_3-edge spectral features.

1.1 ΔeV

The interaction between Fe orbitals and a ligand field removes Fe *3d* orbital degeneracy and gives rise to ligand field splitting parameters such as Δ_t and Δ_o. A measure of the ligand field splitting is given by the relativistic term 10Dq, which is derived from UV-

250 visible spectroscopy. Charge transfer multiplet calculations (using CTM4XAS software)
251 reveals that the XANES L-edge ΔeV has a strong positive correlation (r^2 = 0.98, data not
252 shown) with the ligand field splitting 10Dq parameter, indicating that factors that increase
253 the ligand field splitting (e.g., 10Dq) will similarly increase the X-ray ΔeV value. This
254 relationship is further supported by the positive correlation between measured optical
255 10Dq values (Sherman and Waite, 1985) and the measured ΔeV values for the Fe oxide
256 and –oxy-hydroxide minerals with Fe in octahedral coordination (r^2 = 0.64, Table 1). The
257 differences between the optical 10Dq value and the X-ray ΔeV (Table 1; 10Dq greater
258 than ΔeV by ~12 – 25%) do not agree well with the theoretical calculations that predict
259 that for 10Dq values less than 1.98; the 10Dq value should be less than the ΔeV value.
260 This offset does however agree well with previous work conducted on the high-spin
261 Mn(II) system (Cramer et al., 1991) which showed that the X-ray data reflects the crystal
262 field strength in the final state (i.e., not the ground state), and the decreased splitting
263 measured by X-ray techniques may be attributed to core-hole effects (Cramer et al.,
264 1991).
265
266 Because of their strong impacts on the ligand field splitting parameter and because of the
267 positive relationship between 10Dq and ΔeV, Fe valence state and Fe coordination
268 number represent first order impacts on the magnitude of the ΔeV value. Fe(II) phases
269 show a larger degree of variability in their ΔeV value (1.1 – 2.8 eV (Fig. 3a)), with Fe(II)
270 silicates in particular showing the highest values (2.2 – 2.8 eV). The Fe(III) system is
271 relatively more constrained; comprising of ΔeV values ranging between 1.3 – 2.0 eV,
272 with the majority of common Fe-oxides in the range of 1.4 – 1.7 eV. The coordination

273 environment, specifically the coordination number (CN), is known to impact directly on
274 the degree of ligand field splitting (e.g., $\Delta_t = {}^4/_9\Delta_o$; Fig. 1c); and is thus expected to impact
275 on the magnitude of the ΔeV value. This is confirmed by an analysis of the polymorphs
276 of the Fe(III)PO_4 system. Heterosite, the octahedral-coordinated Fe(III) PO_4 polymorph
277 (CN = 6), has a measured ΔeV value of 1.59 (Augustsson et al., 2005) whereas its
278 tetrahedral counterpart (CN = 4), rodolicoite, has a much lower ΔeV value (0.34; de
279 Groot et al., 2005) and is characterised by a weak low energy feature.
280
281 Ligand effects, which can influence the extent of ligand field splitting, play a second
282 order role in impacting spectral ΔeV values. Specifically, the spectrochemical series can
283 be used as a semi-quantitative measure in determining the relative ligand field splitting
284 with strong field ligands such as SO_4^{2-} (ΔeV = 1.58 – 1.65 (Shirakawa et al., 2007; Peak
285 et al., 2012) displaying the high ΔeV whereas weak field ligands such as NO_3^- (ΔeV =
286 1.41 (Peak et al., 2012) have lower values. To exclude ligand-specific effects, additional
287 comparisons were made using only the spectral parameters of the polymorphs of the Fe
288 oxide and oxy-hydroxide system, where the only ligands are O^{2-} and OH^-. Despite the
289 chemical similarities between these two ligands (i.e., both form partially covalent Fe-O
290 bonds through hybridisation of O *2p* and Fe *3d* orbitals), the hydrogen present in the
291 hydroxyl (OH^-) ligand significantly affects the electron density around the bonding
292 oxygen (Welsh and Sherwood, 1989), and thus the ionicity of metal-ligand bonds
293 (Sherman, 1985). This effect has a stronger impact on the binding energies associated
294 with O *1s* or *2s* electronic transitions to valence orbitals (Welsh and Sherwood, 1989;
295 Gilbert et al., 2007), yet it also affects the structure of the valence orbitals, notably

296 leading to an increase in the ligand field splitting (Fig. 1c). These small-scale shifts in the
297 spectral parameters (e.g., ΔeV) due to subtle changes in the covalency of the oxygen-
298 metal bonds could not be precisely reproduced using the CTM4XAS software.
299
300 Because Fe L-edge spectroscopy probes only the local coordination environment (van der
301 Laan and Kirkman, 1992); additional differences in the measured ΔeV values in the iron
302 oxide and iron oxy-hydroxide system must be related to variations in the coordination
303 polyhedra. The crystal structure of the different polymorphs dictate the geometry (and
304 thus site symmetry), and number and type (face-, edge- or point-sharing) of linkages
305 associated with the local Fe coordination polyhedra (Fig. 4). Several of the minerals
306 consist of multiple Fe coordination sites (Fig. 4: akaganeite, ferrihydrite, maghemite,
307 magnetite) and each polyhedron is associated with its own degree of distortion and
308 decline in symmetry away from perfect octahedral symmetry. The experimental XANES
309 spectrum (from the bulk Fe oxide or –oxy-hydroxide) reflects the spectral contributions
310 from each of these polyhedra. Although theoretical calculations can reproduce the
311 splitting of the Fe L_3-edge, accurate theoretical calculation of the fine structure associated
312 with structural variations and symmetry declines across multiple Fe sites will be
313 challenging to calculate as each distorted polyhedron will be characterised by its own
314 multiplicity, peak shifts and line-broadenings. The experimental spectra, however, show
315 the net effects of all of the structurally-controlled distortions and these third order effects
316 result in ΔeV shifts of around 0.12 eV (Figs. 3b; 4).
317

Figure 5 summarizes the relationship between spectral parameters and a number of properties of Fe coordination polyhedra in Fe oxides and oxy-hydroxides (averaged if more than one Fe site was present). Angle variance and quadratic elongation are distortion measures relating respectively to the deviations in ligand bond angle and bond length away from those associated with an ideal polyhedron (Robinson et al., 1971); whereas volume distortion percentage is measured relative to the volume of an ideal polyhedron (Makovicky and Balic-Zunic, 1998; Balic-Zunic, 2007). The ΔeV spectral parameter displays a strong positive correlation with bond-angle variations and volume distortion of the polyhedron while it exhibits a strong negative correlation with variability in ligand bond length. Comparison between the polyhedral volume distortion and the ΔeV value yields a strong positive correlation. The number and types of polyhedral linkages also influence the local bonding environment within the Fe coordination polyhedron. The ΔeV value shows only moderate and negative correlation to the total number of polyhedral linkages with the prevalence of edge-sharing linkages over corner-sharing linkages favouring higher ΔeV values. Finally, additional distortion effects can occur for example, with the presence of trace impurities. These distortion effects can exert profound influence the geometry and point group symmetry of coordination polyhedra, with the ability to remove degeneracy of molecular orbitals (Fig. 1c; Sherman, 1985a). Such multiplet effects can lead to spectral peak broadening and shifts in the ΔeV value, depending on the composition of the orbitals resulting from distorted symmetry.

1.2 Intensity Ratio

341 The intensity ratio of the constituent split peaks of the Fe L_3-edge spectrum have
342 traditionally been used in the determination and quantification of Fe valence state
343 (Cressey et al., 1993; van Aken et al., 2002; Miyajima et al., 2004; Calvert et al., 2005;
344 Cavé et al., 2006; Dynes et al., 2006; Liu et al., 2015). This is because the Fe oxidation
345 state, and the corresponding number of vacancies in the valence orbitals, exert the
346 strongest control on Fe L_3-edge intensity ratio (Fig. 3a). An intensity ratio of ~1 can be
347 used to clearly differentiate between the Fe(III) species and Fe(II) species, the former
348 having an intensity ratio around 0.51 (±0.18) whereas the latter averages around 2.00
349 (±1.50). Mixed valence species have an intensity ratios closer to 0.7 (±0.30). From
350 theoretical calculations, the strength of the ligand field (as measured by the 10Dq value)
351 also has a strong influence on the intensity ratio value (i.e., for O_h symmetry with Slater
352 integrals set to 70% (e.g., Miedema and de Groot, 2013) the correlation coefficient (r^2)
353 between the intensity ratio and 10Dq is 0.99). Additional first order influences on the
354 number of orbital vacancies, and thus the L_3-edge intensity ratio, include the coordination
355 number (O_h versus T_d) and the spin state (high spin versus low spin) of the Fe species.
356
357 Second order influences on the intensity ratio value are attributed to ligand effects on the
358 chemical character of available singly-occupied and unoccupied molecular orbitals. In
359 accordance with the Laporte selection rule (Burns, 1970), it is particularly the amount of
360 Fe d-character (or conversely, the amount of ligand p-character) in these valence orbitals
361 that determines the likelihood of dipole-allowed *2p→3d* electronic transitions. In their
362 work on differential orbital covalency in Fe chelators, the L-edge splitting data of
363 Hocking et al. (2010) showed good correlation with both the bond length (affected by

364 bond covalency/ionicity) and the % d-character (inversely proportional to bond
365 covalency) in valence orbitals (Table 2). Bond covalency is closely tied to π-bonding
366 interaction which occurs exclusively between ligand p-orbitals and the Fe *3d* t_{2g} subset of
367 orbitals. If the low and high energy peaks in the Fe L_3-edge spectrum are tentatively
368 assigned t_{2g} and e_g character respectively, then changes in the overall bond covalency, a
369 ligand-specific effect, will impact on the observed spectral intensity ratio. Ligand effects
370 influence the intensity ratio by up to a value of 0.2 when ligands are similar (e.g. O^{2-} vs
371 OH^-, Fig. 3b), and this influence can exceed 0.4 when ligands are vastly different (S^{2-}: 0.8
372 (Bornite (Miklin et al., 2005)) versus NO_3^-: 0.4 (Peak and Regier, 2012)).
373
374 Polyhedral distortion also affects the orbital composition by inducing multiplet structure
375 in which the ligand *p*-character is further split among orbitals at different energy levels.
376 Applying the Robinson et al. (1971) scheme which uses quadratic elongation and
377 variance of bond angles to measure polyhedral distortion; we find that the intensity ratio
378 values for species from the Fe –oxide and oxy-hydroxide do not correlate with variations
379 in bond angle and show only relatively weak positive correlation with the changes in
380 bond length (Fig. 5a). The correlation between intensity ratio value and the volume
381 distortion percentage is negative (r^2 = 0.59, Fig. 5c), indicating that high ratios result
382 from low polyhedral distortions. The intensity ratio shows better correlation with the
383 number and type of polyhedral linkages experienced between adjacent Fe coordination
384 polyhedra. Large intensity ratios are strongly favoured as the number of polyhedral
385 linkages increases, particularly when the proportion of corner-sharing linkages increases
386 preferentially (Fig. 5a). Figure 5 additionally alludes to the inverse relationship between

ΔeV and intensity ratio, indicative that the third order impacts that lead to high ΔeV also typically result in lower intensity ratio values.

2. Application of L_3-edge XAS to Fe-oxide and oxy-hydroxide speciation

The sensitivity of the Fe $L_{2,3}$-edge to local coordination (i.e. variations in ligand arrangement and type) renders it an ideal probe to investigate Fe mineralogy and to derive chemical and structural information from amorphous Fe phases. Figure 3b plots the spectral parameters (ΔeV and intensity ratio) of Fe oxide and oxy-hydroxide mineral standards ranging in size between 20 nm and 400 nm. The spectral parameters did not show any size-dependent trends in their magnitudes. The plot is limited to the Fe-O and Fe-OH system to limit any additional ligand-specific effects on the spectral parameters (e.g. electronegativity, ionic size and charge, and specific bonding interaction). Each solid square represents the average ΔeV and intensity ratio value for each standard phase, and these averages were calculated by considering only the 299 environmentally-relevant spectra (i.e., only spectra with an L_3-edge high energy peak maximum of between 0.17 and 0.83), to limit saturation effects associated with transmission mode XANES. Despite constraining this range, some saturation was still observed and resulted in the broader horizontal error bars associated with the intensity ratio averages (Fig. 3b) relative to the error bars associated with the ΔeV values (both sets of error bars represent 1 x standard deviation). The measured spectral parameters for the various phases are reported in the format *intensity ratio (± intensity ratio standard deviation): ΔeV (± ΔeV standard deviation*) and are; amorphous Fe oxy-hydroxide (*0.51 ± 0.02: 1.50 ± 0.02*); goethite (*0.52 ± 0.04: 1.54 ± 0.02*); akaganeite (*0.47 ± 0.02: 1.54 ± 0.04*); lepidocrocite (*0.48 ±*

410 *0.03: 1.65 ± 0.03*); hematite (*0.66 ± 0.06: 1.52 ± 0.06*); and maghemite (*0.55 ± 0.07: 1.43*
411 *± 0.06*). The magnetite point is plotted from data collected from a single standard
412 spectrum (intensity ratio- 0.72; ΔeV- 1.14) and the associated error bars are estimated
413 from the average of the standard deviations found in the other six data points. The
414 magnetite spectral shape and position of this field on the plot matches well with other
415 published data (Kendelewicz et al., 2000; Regan et al., 2001; de Smit et al., 2009; Zhu et
416 al., 2015). A series of two-tailed t-tests (95 % confidence limit) was conducted on these
417 averages, and all data points are significantly different from one another in terms of the
418 combinations of their ΔeV and intensity ratio values.
419
420 The most noticeable controls on the phase distribution in the plot are the first order and
421 second order effects of coordination number and ligand type respectively. Mineral phases
422 characterised by the presence of tetrahedral iron (magnetite (Fig. 4j), maghemite (Fig.
423 4m), and possibly ferrihydrite (Fig. 4g; Michel et al., 2007; Peak and Regier, 2012;
424 Guyodo et al., 2012) typically have the lowest values for ΔeV. This is in agreement with
425 the generalized chemical trend for ligand field splitting in which $\Delta_t = {}^4/_9\Delta_o$ (e.g. Burns,
426 1970) (Fig. 1c). Although the number of different types of ligands has been limited in this
427 dataset, the presence of hydroxyl ligands causes marked shifts in the molecular orbital
428 structure of Fe polyhedra (Fig. 1c: $FeO_4(OH)_2^{7-}$ octahedron). The presence of the
429 hydroxyl ligands in the FeOOH mineral structure also results in lower intensity ratio
430 values (<0.55), relative to pure oxide phases (intensity ratio greater than 0.55; Fig. 3).
431 The lower intensity ratio values in Fe oxy-hydroxide phases indicate that bonding to
432 hydroxyl groups results in modifications to the valence orbital compositions, making

433 transitions to the high energy orbitals relatively more favourable. For example, Sherman
434 (1985) found that hydroxyl ligands appear to promote the covalency between Fe^{3+} centres
435 and O^{2-} oxygens. Following the discussion in section 1.2., this will result in more O *2p*
436 character in the t_{2g} valence orbital subset making the electronic transitions less allowable,
437 and thus decreasing the observed intensity ratio in Fe oxy-hydroxides (Fig. 3b).
438
439 On account of their polymorphism, the Fe oxy-hydroxides have equivalent chemical
440 stoichiometry and are closely grouped on the ΔeV versus intensity ratio diagram. Third
441 order distortion effects need to be invoked to explain the small differences in their
442 distribution on the plot. Goethite (α-FeOOH) has a tunnel structure (Cornell and
443 Schwertmann, 2003) characterised by a single type of Fe octahedron showing only
444 moderate percentage volume distortion (Fig. 4a). Distortion in the goethite octahedron is
445 caused by differences in the coordinating ligand (e.g., Fig. 4a: longer hydroxyl oxygen
446 bond distances: 2.072 – 2.097 Å versus shorter oxygen group bond distances 1.928 –
447 1.955 Å) and by variations in the type of linkages to adjacent Fe octahedra (e.g. the
448 longest bonds are between the Fe centre and hydroxyl ligands that are shared by two
449 adjacent edge-sharing octahedra).
450
451 Akaganeite is structurally similar to its polymorph goethite as they both have equal
452 number and types of polyhedral linkages between adjacent octahedra. It is thus not
453 surprising that their fields in the ΔeV versus intensity ratio plot are close and partially
454 overlap. There is insignificant difference in the degree of splitting in the valence orbitals
455 (both ΔeV values ~ 1.54) and their plotted fields are thus only offset by a difference in

456 intensity ratio of ~0.05. Although the spectral interpretation of akaganeite may be slightly
457 complicated by the presence of chloride ions and two structurally different Fe sites, the
458 relationships shown in figure 5 should still be explored when explaining the observed
459 shift in intensity ratio. The relationship between goethite intensity ratio (0.52) and
460 akaganeite intensity ratio (0.47) does not conform to the trends in the either the angle
461 variance or the quadratic elongation distortion parameters, both of which are only weak
462 to moderate trends. The higher averaged volume distortion in the akageneite octahedra
463 relative to the goethite octahedron is in good agreement with the strong negative
464 correlation between intensity ratio and percentage volume distortion (Fig. 5c). The effect
465 of volume distortion may be larger than alluded to by the average value reported for the
466 akaganeite structure, as the resolved values for each centre show that the akaganeite Fe1
467 octahedron has the highest degree of volume distortion for any of the Fe oxide or oxy-
468 hydroxide polyhedra (Fig. 4c).
469
470 Lepidocrocite differs from its polymorphs in that it has a layered structure and each Fe
471 octahedron consists of only two hydroxyl groups. Mineral stoichiometry is achieved by
472 the linkage arrangement between adjacent polyhedra, as each hydroxyl group is only
473 shared by one edge-sharing octahedron whereas each oxygen ligand is shared by two
474 adjacent Fe octahedra. This low proportion of corner-sharing linkage interactions is one
475 reason that lepidocrocite has a higher ΔeV value than its polymorphs (Figs. 4, 5). The
476 increased ΔeV value relative to its polymorphs is in agreement with previous studies that
477 have shown lepidocrocite to have a higher degree of crystal field splitting (Sherman and
478 Waite, 1985). The degree of polyhedral distortion likely compounds the effects of the low

479 percentage of corner sharing polyhedra and can further be used to explain the observed
480 high ΔeV value. This is true for all three distortion parameters as lepidocrocite has a high
481 angle variance (+ correlation to ΔeV), the lowest quadratic elongation value (- correlation
482 to ΔeV) and the highest volume distortion percentage (+ correlation to ΔeV). The average
483 lepidocrocite intensity ratio value (0.48) is very similar to that of akaganeite and its
484 dissimilarity to the goethite value can only be attributed to the differences in volume
485 distortion percentage and the percentage of corner sharing polyhedra.
486
487 The Fe oxide side of the plot (intensity ratio > 0.55) consists of the polymorphs of the
488 Fe_2O_3 system and the mixed valence phase magnetite. The magnetite point is plotted
489 from data collected from only one spectrum and the associated error bars are estimated
490 from the average of the standard deviations found in the other six data points. The
491 magnetite spectral shape and position of this field on the plot matches well with other
492 published data (Kendelewicz et al., 2000; Regan et al., 2001; de Smit et al., 2009; Zhu et
493 al., 2015). Magnetite has a low ΔeV value, largely attributable to the presence of
494 tetrahedral Fe(III)- which has a low degree of crystal field splitting relative to octahedral
495 Fe(III) (Fig. 1c). The low volume distortion in the polyhedra can further lower the
496 observed ΔeV value, as can the large percentage of corner-sharing linkages (Fig. 4i, j).
497 Magnetite has the highest intensity ratio due to structural Fe(II), the absence of hydroxyl
498 ligands, a high number adjacent polyhedra and a large proportion of the polyhedral
499 linkages connecting via corner-shared oxygen atoms.
500

501 Maghemite and hematite are both polymorphs of Fe_2O_3 with the former having a cubic
502 crystal structure and the latter belonging to the trigonal crystal system. Spectral
503 interpretation of the maghemite data points may be complicated by the presence of three
504 different types of Fe sites (Fig. 4k-m), which can lead to additional multiplicity in the
505 number and energies of the transitions to valence orbitals. Despite being structurally
506 similar to magnetite, the maghemite point plots away from the magnetite point on the
507 ΔeV versus intensity ratio plot (Fig. 3b). Although both phases have low ΔeV values due
508 to the presence of tetrahedral Fe, the magnetite ΔeV value (1.13) is lower than the
509 maghemite ΔeV value (1.43). Hematite has a larger ΔeV value than the other two Fe
510 oxide minerals, and this may be partially attributed to the prevalence of face-sharing
511 linkages between adjacent polyhedral (i.e., lower % corner-sharing linkages). Additional
512 support for the positioning of hematite above maghemite on the ΔeV scale is given by
513 hematite's higher angle variance, lower quadratic elongation and higher percentage
514 volume distortion. Aside from the absence of hydroxyl groups, the major factors
515 increasing the intensity ratio of the oxide phases relative to the oxy-hydroxides, is the
516 higher total number of polyhedral linkages associated with each Fe polyhedron and the
517 enhanced proportion of these being corner-sharing linkages.
518
519 Amorphous iron oxy-hydroxide, or ferrihydrite, plots with a ΔeV value of 0.51 ±0.02 and
520 an intensity ratio value of 1.50±0.02. The position of this field on the ΔeV versus
521 intensity ratio plot may render some insights into the controversy that currently ensues
522 over the structure of ferrihydrite (Jambor and Dutrizac, 1998; Janney et al., 2001; Michel
523 et al., 2007; Peak and Regier, 2012; Manceau, 2012; Gilbert et al., 2013). Amorphous Fe

524 oxy-hydroxide has an intensity ratio that is less than 0.55, suggesting that a proportion of
525 the ligands present in the local coordination environment are hydroxyl groups. The
526 amorphous Fe oxy-hydroxide field plots closest to goethite suggesting a degree of
527 structural similarity between the two phases, particularly that amorphous Fe oxy-
528 hydroxide is likely to have a more contained structure relative to the layered
529 lepidocrocite. Because of its greater intensity ratio compared to lepidrocrocite and
530 akaganeite, amorphous Fe oxy-hydroxide is likely to have a lower degree of average
531 percentage volume distortion than these two minerals. The ΔeV value for amorphous Fe
532 oxy-hydroxide plots in the lower range of ΔeV values; and low ΔeV values are more
533 strongly associated with the Fe oxide phases (e.g., maghemite, magnetite) than with Fe
534 oxy-hydroxide phases. This suggests that other structural properties are responsible for
535 the decreased ΔeV value. Plausible structural explanations for the lowered ΔeV value
536 include the presence of tetrahedral Fe, a lower proportion of hydroxyls than is found in
537 oxy-hydroxide structure, or that there is a lower average volume distortion in each
538 polyhedron (e.g., characterized by more variable bond lengths but less variable bond
539 angles).
540
541 Comparing these theorised characteristics to the reported structure for ferrihydrite
542 proposed by the Michel model (Fig. 4e-g); we find a good agreement. Their model
543 reports a presence of 10-20% structural Fe(III) in tetrahedral coordination, although
544 subsequent Fe L-edge work has suggested that the amount of tetrahedral Fe(III) could be
545 as high as 40% (Peak and Regier, 2012). Because our amorphous Fe oxy-hydroxide ΔeV
546 value is larger than the maghemite ΔeV value, an explanation based solely on the

547 presence of tetrahedral Fe(III) would then argue for a lower percentage contribution of
548 Fe(III) in tetrahedral coordination, in agreement with data from Michel et al., 2007. The
549 Michel model, which is based on the structure of the mineral akdalaite ($Al_{10}O_{14}(OH)_2$),
550 suggests that the ferrrihydrite chemical formula is $Fe_{10}O_{14}(OH)_2$. This presence of
551 hydroxyl ligands can explain the low (<0.55) intensity ratio observed in our results, and a
552 low proportion of hydroxyl ligands relative to oxygen ligands (e.g., less than the 50:50
553 ratio associated with goethite) may also be (partially) causative for the lower ΔeV value
554 (Fig. 1c). This is in agreement with recent work conducted by Gilbert et al. (2013) who
555 have suggested a 'hybrid' structural model for ferrihydrite characterised by a significantly
556 lower proportion of structural hydroxyls than is found in goethite. Distortion effects can
557 cause third order variations to the ΔeV values; particularly, an increase in %volume
558 distortion favours higher ΔeV values (Fig. 5a). However, the average percentage volume
559 distortion for ferrihydrite (2.21%), predicted by the Michel model, is higher than for the
560 goethite and akaganeite distortion values (Fig. 4a, c-g). This indicates that this distortion
561 effect cannot be responsible for the observed low ΔeV value, thereby highlighting the
562 importance of the other chemical factors (e.g. tetrahedral Fe and the presence of
563 hydroxyls) in explaining our observed results.
564

565 **3. Implications**

566

567 The high spectral and spatial resolution associated with Fe L_3-edge spectroscopy provides
568 an ideal probe for investigating mineralogical and chemical variations in small (sub-μm
569 sized) particles. The technique is particularly well-suited to natural samples because the

570 analytical conditions (soft X-ray probe; 1 atm. *P*; ambient *T*) ensure that the sample
571 integrity is maintained. Because the Fe L_3-edge can be parameterised into the ΔeV
572 (reflecting the energy difference between the valence orbital sets) and the intensity ratio
573 value (reflecting the chemical composition of the valence orbital sets), the discrete fields
574 occupied by Fe minerals on the ΔeV vs. intensity ratio plot reflect important molecular-
575 level chemical variations characteristic of the coordination polyhedra of different Fe
576 mineral phases. The plot is thus a useful tool for investigating the chemistry and
577 mineralogy of sub-micrometer sized particles in a diverse array of environments (e.g.,
578 aerosols, fluvial and marine colloids, soil systems).
579
580 Our previous work has applied this tool to study Fe particle speciation in the South
581 Atlantic and Southern Oceans (von der Heyden et al., 2012), where Fe biogeochemistry is
582 an important driver of primary productivity (i.e., representing the biological conversion
583 of the green-house gas CO_2 to phytoplankton biomass). We have also used the ΔeV vs.
584 intensity ratio plot to show that ferrous colloids are stable in oxygenated fluvial,
585 lacustrine and marine surface waters; and that these Fe(II) colloids have a meaningful
586 association with carboxamide functional groups present in organic matter (von der
587 Heyden et al., 2014). These examples showcase the applicability of the plot towards
588 understanding Fe mineral speciation; and it is foreseen that the plot will continue to
589 render invaluable insights into Fe mineralogy in diverse environments, particularly as
590 scientists increasingly probe the role of Fe phases in the sub-micrometer size domain
591 (e.g., Fe nanoparticle research (Wiggington et al., 2007)).

592 **ACKNOWLEDGEMENTS**

593

594 This research is supported by grants from NRF, South Africa (Blue Skies Program),
595 Stellenbosch University VR(R) fund, NSF (chemical sciences), US-DOE (BES & SBR),
596 and Princeton University. The authors would like to thank the support staff at the
597 Advanced Light Source for helping with data collection and sample preparation and L.
598 Barbour for his help with the crystallographic program XSeed.

599

REFERENCES

Appelo, C.A.J., and Postma, D. (2004) Geochemistry, groundwater and pollution. CRC press, 649 pp.

Atwood, J.L., and Barbour, L.J. (2003) Molecular graphics: from science to art. Crystal Growth & Design, 3, 3.

Augustsson, A., Zhuang, G.V., Butorin, S.M., Osorio-Guillen, J.M., Dong, C.L., Ahuja, R., Chang, C.L., Ross, P.N., Nordgren, J., and Guo J.-H. (2005) Electronic structure of phospho-olivines Li_xFePO_4 (x = 0, 1) from soft-x-ray-absorption and -emission spectroscopies. Journal of Chemical Physics, 123, 184717_1 – 9.

Balic Zunic, T. and Vickovic, I. (1996) IVTON- program for the calculation of geometrical aspects of crystal structures and some crystal chemical applications. Journal of Applied Crystallography, 29, 305 – 306.

Balic Zunic, T. (2007) Use of three-dimensional parameters in the analysis of crystal structures under compression. In: Grzechnik A, editor. Pressure-induced phase transitions. Trivandrum: Transworld Research Network; 157 – 184.

Benzerara, K., Menguy, N., Banerjee, N.R., Tyliszczak, T., Brown, G.E. Jr, and Guyot, F. (2007) Alteration of submarine basaltic glass from the Ontong Java Plateau: A STXM and TEM study. Earth and Planetary Science Letters, 260, 187 – 200.

Blake, R.L., Hessevick, R.E., Zoltai, T., and Finger, L.W. (1966) Refinement of the hematite structure. American Mineralogist, 51, 123 – 129.

Bluhm, H., Andersson, K., Araki, T., Benzerara, K., Brown, G.E., Dynes, J.J., Ghosal, S., Gilles, M.K., Hansen, H.-Ch., Hemminger, J.C., and others (2006) Soft X-ray microscopy and spectroscopy at the molecular environmental science beamline at the Advanced Light Source. Journal of Electron Spectroscopy and Related Phenomena, 150, 86 – 104.

Bourdelle, F., Benzerara, K., Beyssac, O., Cosmidis, J., Neuville, D.R., Brown, G.E., and Paineau, E. (2013) Quantification of the ferric/ferrous iron ratio in silicates by scanning transmission X-ray microscopy at the Fe L2, 3 edges. Contributions to Mineralogy and Petrology, 166, 423 – 434.

Burns R.G. (1970) Mineralogical applications of crystal field theory. Harland W. B., Agrell S. O., Davies D., Hughes H. F., editors. Cambridge University Press.

Calvert, C.C., Brown, A., and Brydson, R. (2005) Determination of the local chemistry of iron in inorganic and organic materials. Journal of Electron Spectroscopy and Related Phenomena, 143, 173 – 187.

Cavé, L., Al, T., Loomer, D., Cogswell, S., and Weaver L. (2006) A STEM/EELS method for mapping iron valence ratios in oxide minerals. Micron, 37, 301 – 309.

Chan, C.S., Fakra, S.C., Edwards, D.C., Emerson, D., and Banfield, J.F. (2009) Iron oxyhydroxide mineralization on microbial extracellular polysaccharides. Geochimica et Cosmochimica Acta, 73, 3807 – 3818.

Chen, K.-F., Lo, S.-C., Chang, L., Egerton, R., Kai, J.-J., Lin, J.-J., and Chen, F.-R. (2007) Valence state map of iron oxide thin film obtained from electron spectroscopy imaging series. Micron, 38, 354 – 361.

639 Chen, C., and Sparks, D.L. (2015) Multi-elemental scanning transmission X-ray microscopy–near edge X-
640 ray absorption fine structure spectroscopy assessment of organo–mineral associations in soils from
641 reduced environments. Environmental Chemistry, 12, 64 – 73.

642 Cornell, R.M., and Schwertmann, U. (2003) The iron oxides: Structure, properties, reactions, occurrences
643 and uses. Weinheim, New York, Basel, Cambidge, Tokyo: VCH.

644 Cramer, S.P., DeGroot, F.M.F., Ma, Y., Chen, C.T., Sette, F., Kipke, C.A., Eichhorn, D.M., Chan, M.K.
645 and Armstrong, W.H. (1991) Ligand field strengths and oxidation states from manganese L-edge
646 spectroscopy. Journal of the American Chemical Society, 113, 7937 – 7940.

647 Cramer, S.P., Chen, J., George, S.J., van Elp, J., Moore, J., Tensch, O., Colaresi, J., Yocum, M., Mullins,
648 O.C., and Chen, C.T. (1992) Soft -ray spectroscopy of metalloproteins using fluorescence detection.
649 Nuclear Instruments and Methods in Physics Research Section A, 319, 285 – 289.

650 Cressey, G., Henderson, C.M.B., and van der Laan, G. (1993) Use of L-edge x-ray absorption spectroscopy
651 to characterize multiple valence states of 3d transition metals; a new probe for mineralogical and
652 geochemical research. Physics and Chemistry of Minerals, 20, 111 – 119.

653 Crocombette, J.P., Pollack, M., Jollet, F., Thromat, N., and Gautier-Soyer, M. (1995) X-ray-absorption
654 spectroscopy at the iron $L_{2,3}$ threshold in iron oxides. Physical Review B, 52, 3143 – 3150.

655 de Groot, F.M.F., Grioni, M., Fuggle, J.C., Ghijsen, J., Sawatzky, G.A., and Peterson, H. (1989) Oxygen 1s
656 X-ray-absorption edges of transition-metal oxides. Physical Review B, 40, 5715 – 5723.

657 de Groot, F.M.F., Fuggle, J.C., Thole, B.T., and Sawatzky, G.A. (1990) 2p x-ray absorption of 3d transition
658 metal compounds: An atomic multiplet description including the crystal field. Physical Review B, 42,
659 5459 – 5468.

660 de Groot, F.M.F. (2005) 1s2p resonant inelastic X-ray scattering of iron oxides. Journal of Physical
661 Chemistry B, 109, 20751.

662 de Smit, E., Creemer, J.F., Zandbergen, H.W., Weckhuysen, B.M., and de Groot, F.M.F. (2009) In-situ
663 scanning transmission X-ray microscopy of catalytic materials under reaction conditions. Journal of
664 Physics: Conference Series, 190, 1 – 4.

665 Dynes, J.J., Tyliszczak, T., Araki, T., Lawrence, J.R., Swerhone, G.D.W., Leppard, G.G., and Hitchcock,
666 A.P. (2006) Speciation and quantitative mapping of metal species in microbial biofilms using scanning
667 transmission X-ray microscopy. Environmental Science & Technology, 40, 1556 – 1565.

668 Fleet, M.E. (1986). The structure of magnetite: symmetry of cubic spinels. Journal of Solid State
669 Chemistry, 62, 75 – 82.

670 Gilbert, B., Kim, C.S., Dong, C.-L., Guo, J., Nico, P.S., and Shuh, D.K. (2007) Oxygen K-edge emission
671 and absorption spectroscopy of iron oxyhydroxide nanoparticles. AIP Conference Proceedings 882, 721 –
672 725.

673 Gilbert, B., Katz, K.E., Denlinger, J.D., Yin, Y., Falcone, R., and Waychunas, G.A. (2010) Soft X-ray
674 spectroscopy study of the electronic structure of oxidized and partially oxidized magnetite nanoparticles.
675 Journal of Physical Chemistry C, 114, 21994 – 22001.

676 Gilbert, B., Erbs, J.J., Penn, R.L., Petkov, V., Spagnoli, D., and Waychunas, G.A. (2013) A disordered
677 nanoparticle model for 6-line ferrihydrite. American Mineralogist, 98, 1465 – 1476.

678 Grandjean, F., Waddill, G.D., Cummins, T.R., Moore, D.P., Long, G.J., and Buschow, K.H.J. (1999) A
679 cerium M-edge X-ray absorption and an iron L-edge magnetic circular dichroism study of the $Ce_2Fe_{17-x}M_x$
680 solid solutions, where M is Al and Si. Solid State Communications, 109, 779 – 784.

681 Gualtieri, A.F. and Venturelli, P. (1999) In situ study of the goethite-hematite phase transformation by real
682 time synchrotron powder diffraction. American Mineralogist, 84, 895 – 904.

683 Guyodo, Y., Sainctavit, P., Arrio, M.A., Carvallo, C., Penn, R.L., Erbs, J.J., Forsberg, B.S., Morin, G.,
684 Maillot, F., Lagroix, F., and Bonville, P. (2012) X-ray magnetic circular dichroïsm provides strong
685 evidence for tetrahedral iron in ferrihydrite. Geochemistry, Geophysics, Geosystems, 13, 1 – 9.

686 Hitchcock, A.P. (2008) aXis2000 is written in interactive data language (IDL) and is freely available online
687 for non-commecial use. http://unicorn.mcmaster.ca/aXis2000.html.

688 Hochella, M.F., Moore, J.N., Putnis, C.V., Putnis, A., Kasama, T., and Eberl, D.D. (2005) Direct
689 observation of heavy metal-mineral association from the Clark Fork River superfund complex:
690 Implications for metal transport and bioavailability. Geochimica et Cosmochimica Acta, 69, 1651 – 1663.

691 Hocking, R.K., George, S.D., Raymond, K.N., Hodgson, K.O., Hedman, B., and Solomon, E.I. (2010) Fe
692 L-edge x-ray absorption spectroscopy determination of differential orbital covalency of siderophore
693 model compounds: Electronic structure contributions to high stability constants. Journal of the American
694 Chemical Society, 132, 4006 – 4015.

695 Jambor, J.L., and Dutrizac, J.E. (1998) The occurrence and constitution of natural and synthetic
696 ferrihydrite, a widespread iron oxyhydroxide. Chemical Reviews, 98, 2549 – 2585.

697 Janney, D.E., Cowley, J.M., and Buseck, P.R. (2001) Structure of synthetic 6-line ferrihydrite by electron
698 nanodiffraction. American Mineralogist, 86, 327 – 335.

699 Kendelewicz, T., Liu, P., Doyle, C.S., and Brown, G.E. (2000) Spectroscopic study of the reaction of
700 aqueous Cr(VI) with Fe_3O_4 (111) surfaces. Surface Science, 469, 144 – 163.

701 Krueger, B.J., Grassian, V.H., Cowin, J.P., and Laskin, A. (2004) Heterogeneous chemistry of individual
702 mineral dust particles from different dust source regions: The importance of particle mineralogy.
703 Atmospheric Environment, 38, 6253 – 6261.

704 Labatut, C., Berjoan, R., Armas, B., Shamm, S., Sevely, J., Riog, A., and Molins, E. (1998) Studies of
705 LPCVD Al–Fe–O deposits by XPS, EELS and Mössbauer spectroscopies. Surface and Coatings
706 Technology, 105, 31 – 37.

707 Lead, J.R., and Wilkinson, K.J. (2006) Aquatic colloids and nanoparticles: Current knowledge and future
708 trends. Environmental Chemistry, 3, 159 – 171.

709 Liu, H.C., Xia, J.L., Nie, Z.Y., Zheng, L., Hong, C.H., and Zhao, Y.D. (2015) Iron L-edge and sulfur K-
710 edge XANES spectroscopy analysis of pyrite leached by Acidianus manzaensis. Transactions of the
711 Nonferrous Metals Society of China, 25, 2407 – 2414.

712 Majestic, B.J., Schauer, J.J., and Shafer, M.M. (2007) Application of synchrotron radiation for
713 measurement of iron redox speciation in atmospherically processed aerosols. Atmospheric Chemistry and
714 Physics, 7, 2475 – 2487.

715 Makovicky, E., and Balic Zunic, T. (1998) New measure of distortion for coordination polyhedra. Acta
716 Crystallographica B, 54, 766 – 773.

717 Manceau, A. (2012) Comment on "Direct observation of tetrahedrally coordinated Fe(III) in ferrihydrite".
718 Environmental Science & Technology,46, 6882 – 6884.

719 Michel, F.M., Ehm, L., Antao, S.M., Lee, P.L., Chupas P.J., Liu, G., Strongin, D.R., Schoonen, M.A.A.,
720 Phillips, B.L., and Parise, J.B. (2007) The structure of ferrihydrite, a nanocrystalline material. Science
721 316, 1726 – 1729.

722 Miedema, P.S., and de Groot, F.M.F. (2013) Fe 2p X-ray absorption and electron energy loss spectroscopy.
723 Journal of Electron Spectroscopy and Related Phenomena, 187, 32 – 48.

724 Mikhlin, Y., Tomashevich, Y., Tauson, V., Vyalikh, D., Molodtsov, S., and Szargan, R. (2005) A
725 comparative X-ray absorption near-edge structure study of bornite, Cu_5FeS_4, and chalcopyrite, $CuFeS_2$.
726 Journal of Electron Spectroscopy and Related Phenomena, 142, 83 – 88.

727 Miot, J., Benzerara, K., Morin, G., Kappler, A., Bernard, S., Obst, M., Férard, C., Skouri-Panet, F., Guigner
728 J.-M., Posth, N., and others (2009) Iron biomineralization by anaerobic neutrophilic iron-oxidizing
729 bacteria. Geochimica et Cosmochimica Acta, 73, 696 – 711.

730 Miyajima, N., Langenhorst, F., Frost, D.J., and Yagi, T. (2004) Electron channeling spectroscopy of iron in
731 majoritic garnet and silicate perovskite using a transmission electron microscope. Physics of the Earth and
732 Planetary Interiors, 143-144, 601 – 609.

733 Padmore, H.A., and Warwick, T. (1994) Soft X-ray monochromators for third-generation undulator
734 sources. Journal of Synchrotron Radiation, 1, 27 – 36.

735 Peak, D., and Regier, T. (2012) Direct observation of tetrahedrally co-ordinated Fe(III) in ferrihydrite.
736 Environmental Science & Technology,46, 3163 – 3168.

737 Post, J.E., and Buchwald, V.F. (1991) Crystal structure refinement of akaganeite. American Mineralogist,
738 76, 272 – 277.

739 Regan, T.J., Ohldag, H., Stamm, C., Nolting, F., Lüning, J., Stöhr, J., and White, R.L. (2001) Chemical
740 effects at metal oxide interfaces studied by x-ray-absorption spectroscopy. Physical Review B, 64, 1 – 11.

741 Ressler, T. (1998) WinXAS: A program for X-ray absorption spectroscopy data analysis under MS-
742 windows. Journal of Synchrotron Radiation, 5, 118.

743 Robinson, K., Gibbs, G.V., and Ribbe, P.H. (1971) A quadratic measure of distortion in coordination
744 polyhedra. Science 172, 567 – 570.

745 Schofield, P.F., Henderson, C.M.B., Cressey, G., and van der Laan, G. (1995) 2p X-ray absorption
746 spectroscopy in the earth sciences. Journal of Synchrotron Radiation, 2, 93 – 98.

747 Schwertmann, U., and Cornell, R.M. (2000) Iron oxides in the laboratory: preparation and characterization.
748 2nd Edition, Wiley VCH, 67 – 143.

749 Sherman, D.M. (1985a) The electronic structure of Fe^{3+} coordination sites in iron oxides; applications to
750 spectra, bonding and magnetism. Physics and Chemistry of Minerals, 12, 161 – 175.
751
752 Sherman, D.M. (1985b) SCF-Xα-SW MO study of Fe-O and Fe-OH chemical bonds; Applications to the
753 Mössbauer Spectra and the magnetochemistry of hydroxyl-bearing Fe^{3+} oxides and silicates. Physics and
754 Chemistry of Minerals, 12, 311-314.
755

Sherman, D.M., and Waite, T.D. (1985) Electronic spectra of Fe^{3+} oxides and oxide hydroxides in the near IR to near UV. American Mineralogist, 70, 1262 –1269.

Sherman, D.M. (2005) Electronic structures of iron(III) and manganese(IV) (hydr) oxide minerals: Thermodynamics of photochemical reductive dissolution in aquatic environments. Geochimica et Cosmochimica Acta, 69, 3249 – 3255.

Shirakawa, J., Nakayama, M., Wakihara, M., and Uchimoto, Y. (2007) Changes in electronic structure upon lithium insertion into $Fe_2(SO_4)_3$ and $Fe_2(MoO_4)_3$ investigated by X-ray absorption spectroscopy. The Journal of Physical Chemistry B, 111, 1424 – 1430.

Shmakov, A.N., Kryukova, G.N., Tsybulya, S.V., Chuvilin, A.L., and Solovyeva, L.P. (1995) Vacancy ordering in-Fe_2O_3: Synchrotron x-ray powder diffraction and high-resolution electron microscopy studies. Journal of Applied Crystallography, 28, 141 – 145.

Stavitski, E. and De Groot, F.M. (2010) The CTM4XAS program for EELS and XAS spectral shape analysis of transition metal L edges. Micron, 41, 687 – 694.

Takahama, S., Gilardoni, S., and Russell, L.M. (2008) Single-particle oxidation state and morphology of atmospheric iron aerosols. Journal of Geophysical Research, 113, 1– 16.

Todd, E.C., Sherman, D.M., and Purton, J.A. (2003a) Surface oxidation of pyrite under ambient atmospheric and aqueous (pH=2-10) conditions: Electronic structure and mineralogy from X-ray absorption spectroscopy. Geochimica et Cosmochimica Acta, 67, 881– 893.

Todd, E.C., Sherman, D.M., and Purton, J.A. (2003b) Surface oxidation of chalcopyrite ($CuFeS_2$) under ambient atmospheric and aqueous (pH 2-10) conditions: Cu, Fe L- and O K-edge x-ray spectroscopy. Geochimica et Cosmochimica Acta, 67, 2137 – 2146.

Tossell, J.A., Vaughan, D.J., and Johnson, K.H. (1974) The electronic structure of rutile, wustite and hematite from molecular orbital calculations. American Mineralogist, 59, 319 – 334.

van Aken, P.A., Liebscher, B., and Styrsa, V.J. (1998) Quantitative determination of iron oxidation states in minerals using Fe $L_{2,3}$-edge electron energy-loss near-edge structure spectroscopy. Physics and Chemistry of Minerals, 25, 323 – 327.

van Aken, P.A. and Liebscher, B. (2002) Quantification of ferrous/ferric ratios in minerals: New evaluation schemes of Fe $L_{2,3}$ electron energy-loss near-edge spectra. Physics and Chemistry of Minerals, 28, 188 – 200.

van der Laan, G. and Kirkman, I.W. (1992) The 2p absorption spectra of 3d transition metal compounds in tetrahedral and octahedral symmetry. Journal of Physics: Condensed Matter, 4, 4189 – 4204.

Vaughan, D.J., Tossell, J.A., and Johnson, K.H. (1974) The bonding of ferrous iron to sulphur and oxygen in tetrahedral coordination: a comparative study using SCF Xα scattered wave molecular orbital calculations. Geochimica et Cosmochimica Acta, 38, 993 – 1005.

Von der Heyden, B.P., Roychoudhury, A.N., Mtshali, T.N., Tyliszczak, T., and Myneni, S.C.B. (2012) Chemically and geographically distinct solid-phase iron pools in the Southern Ocean. Science 338, 1199 –1201.

795 von der Heyden, B.P., Hauser, E.J., Mishra, B., Martinez, G.A., Bowie, A.R., Tyliszczak, T.,
796 Roychoudhury, A.N., and Myneni, S.C.B. (2014) Ubiquitous presence of Fe(II) in aquatic colloids and its
797 association with organic carbon. Environmental Science & Technology Letters, 1, 387 – 392.
798
799 Von der Heyden, B.P., Roychoudhury, A.N. (2015) Application, chemical interaction and fate of iron
800 minerals in polluted sediment and soils. Current Pollution Reports, 1(4), 1 – 15.

801 Wang, H., Peng, G., Miller, L.M., Scheuring, E.M., George, S.J., Chance, M.R., and Cramer, S.P. (1997)
802 Iron L-edge X-ray absorption spectroscopy of myoglobin complexes and photolysis products. Journal of
803 the American Chemical Society, 119, 4921– 4928.

804 Welsh, I.D., and Sherwood, P.M.A. (1989) Photoemission and electronic structure of FeOOH:
805 Distinguishing between oxide and hydroxide. Physical Review B,40, 6386 – 6392.

806 Wiggington, N.S., Haus, K.L., and Hochella, M.F. (2007) Aquatic environmental nanoparticles. Journal of
807 Environmental Monitoring, 9, 1306 –1316.

808 Wycoff, R.W.G. (1963) 2nd edition, Interscience Publishers, New York, Crystal Structures 1, 290 – 295.

809 Zhu, X., Kalirai, S.S., Hitchcock, A.P., and Bazylinski, D.A. (2015) What is the correct Fe L_{23} X-ray
810 absorption spectrum of magnetite? Journal of Electron Spectroscopy and Related Phenomena, 199, 19 –
811 26.

Figure Captions

Fig. 1a. *Fe $L_{2,3}$-edge XANES spectra of the iron oxides and iron oxy-hydroxides evaluated in this study. The ΔeV value is measured as the energy difference between the positions of the maxima of the two main peaks in the L_3-edge, whereas the intensity ratio is given by the quotient of the respective peaks' maxima (i_1/i_2). The bars indicate the probabilities of theoretically calculated electronic transitions (CTM4XAS software) occurring for an Fe(III) metal centre in O_h symmetry with 10Dq set to 1.45 and Slater integrals set to 70% (after Miedema and de Groot, 2013).* ***1b:*** *Molecular orbital diagram highlighting the Fe $2p_{3/2}$ electronic transitions to the t_{2g} and e_g valence orbital subsets. The energy difference between these subsets strongly affects the observed spectral splitting ΔeV (Fig. 1a).* ***1c:*** *Variations in local coordination environment around the Fe centre can induce additional loss in the degeneracy in the valence orbitals and shifts in their relative energy positions (reflected in ΔeV). Modelled energy level data is from Sherman, 1985a (FeO_6^{9-} O_h; FeO_6^{9-} C_{3v} (trigonal distortion) and FeO_4^{5-} T_d); Sherman, 1985b ($FeO_4(OH)_2^{7-}$); Tossell et al., 1974 (FeO_6^{10-}); Vaughan et al., 1974 (FeO_4^{6-}) and Burns, 1970 (Fe(II) octahedra with D_{4h} (elongated along tetrad axis); C_{3V} (compressed along tetrad axis) and C_2 (monoclinic) symmetries). Modelled energy levels (excluding those from Burns, 1970) are normalised to the energy scale of Sherman, 1985b.*

Fig. 2: *Theoretical calculations to reproduce the subtle shifts in ΔeV and intensity ratio (as observed in our experimental spectra of the Fe oxide and Fe-oxy-hydroxide mineral standards) are complicated by the sheer number of parameters that can influence the magnitude of these two spectral parameters. All data generated in CTM4XAS software by varying crystal field parameters and Slater integral reductions associated with an Fe^{3+} metal centre in octahedral coordination (i.e., spin orbit coupling and charge transfer parameters were not considered in generating this plot). Number ranges on plot represent the range indicated by the plotted points (usually in increments of either 0.02 or 0.1).*

Fig. 3a: *ΔeV versus intensity ratio plot of spectral parameters of various published Fe phases. An intensity ratio of ~1 can be used to distinguish between Fe(II)-rich and Fe(III)-rich phases (adapted from von der Heyden et al., 2012- see original for all references).* ***3b:*** *ΔeV versus intensity ratio plot for the Fe oxide and Fe oxy-hydroxide system, showing how characteristic spectral features can be used to differentiate between phases with differing structure and chemistry. Error bars reflect one times standard deviation.*

Fig. 4: *Iron polyhedra with local coordination for the Fe oxide and oxy-hydroxide mineral phases analyzed in this study. Polyhedral distortions are the result of chemical and mineralogical (i.e. number and type of polyhedral linkages) properties of the respective phases. Inset octahedra are relative to a perfect octahedron and give an idea of the bond angle distortions and volume distortion (% volume distortion measure indicated in bold). All bond lengths are in Angstrom units (Å) and all images were generated using XSeed (Atwood and Barbour, 2003) and crystallographic data from published references: [1]Gualtieri et al., 1999; [2]Wyckoff, 1963; [3]Post and Buchwald, 1991; [4]Michel et al., 2007; [5]Blake et al., 1966; [6]Fleet, 1986; [7]Shmakov et al., 1995.*

Fig. 5a: *Goodness of fit plot obtained from r^2 values derived from comparisons between spectral parameters and various structural and distortion parameters. Plus and minus symbols refer to positive and negative correlations respectively.* ***5b:*** *Volume distortion percentage versus ΔeV and,* ***5c:*** *volume distortion percentage versus intensity ratio plots for polyhedra from the Fe oxide*

and oxy-hydroxide system. Trend lines reflect the degree of correlation between the respective parameters.

Tables

Table 1: Comparison between various methods for determining d-orbital splitting

Species	ΔeV (STXM)	Optical 10Dq	Oxygen K-edge
Goethite	1.54[1]	1.90[2]	-[a]
Lepidocrocite	1.65[1]	1.98[2]	-[a]
Hematite	1.53[1]	1.74[2]	1.41[3]
Maghemite	1.43[1]	1.91[2]	0.91[4]

[1]Our data, [2]Sherman and Waite (1985), [3]Sherman (2005), [4]Gilbert et al. (2010). [a]Presence of both oxo- and hydroxyl ligands prevents direct determination of orbital splitting from the oxygen K-edge. Dataset limited to the Fe-oxide and oxy-hydroxide system because of the scope of this study and because 10Dq values for Fe-silicate species are difficult to estimate due to low symmetry and trace impurities (Burns, 1970). Data for maghemite (γ-Fe_2O_3) may be complicated by the presence of Fe in both octahedral (O_h) and tetrahedral (t_d) sites.

Table 2: Intensity ratio correlation to bond length and orbital character in organic Fe (III) chelates

Species	Intensity Ratio	Average bond length (Å)	Average % d-character in valence orbitals
$[Fe(ox)_3]^{3-}$	0.49	2.008	84
$[Fe(pha)_3]$	0.43	2.013	68
$[Fe(cat)_3]^{3-}$	0.39	2.017	65
	Correlation R^2 value:	0.997 (-)	0.934 (+)

*** All data after Hocking et al. (2010)*

Figures

Figure 1:

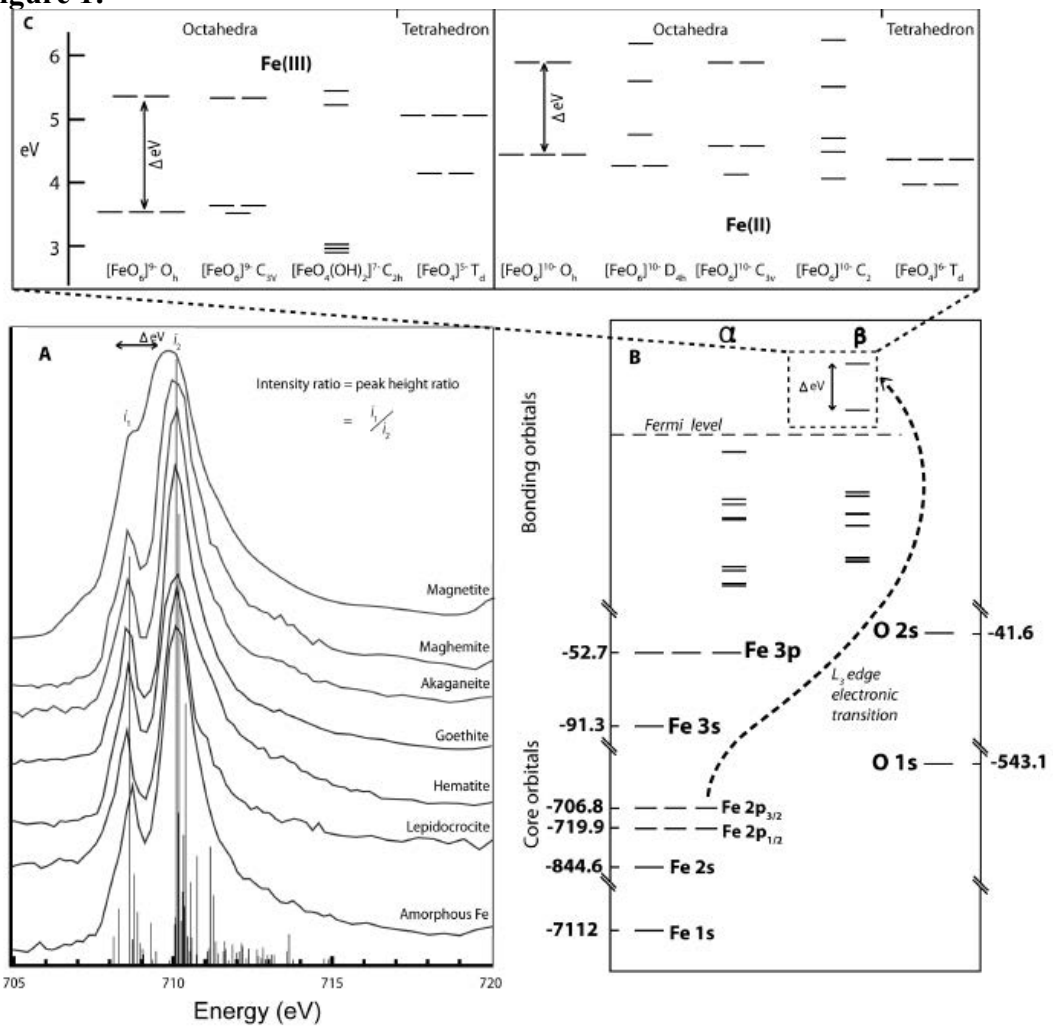

886 **Figure 2:**
887

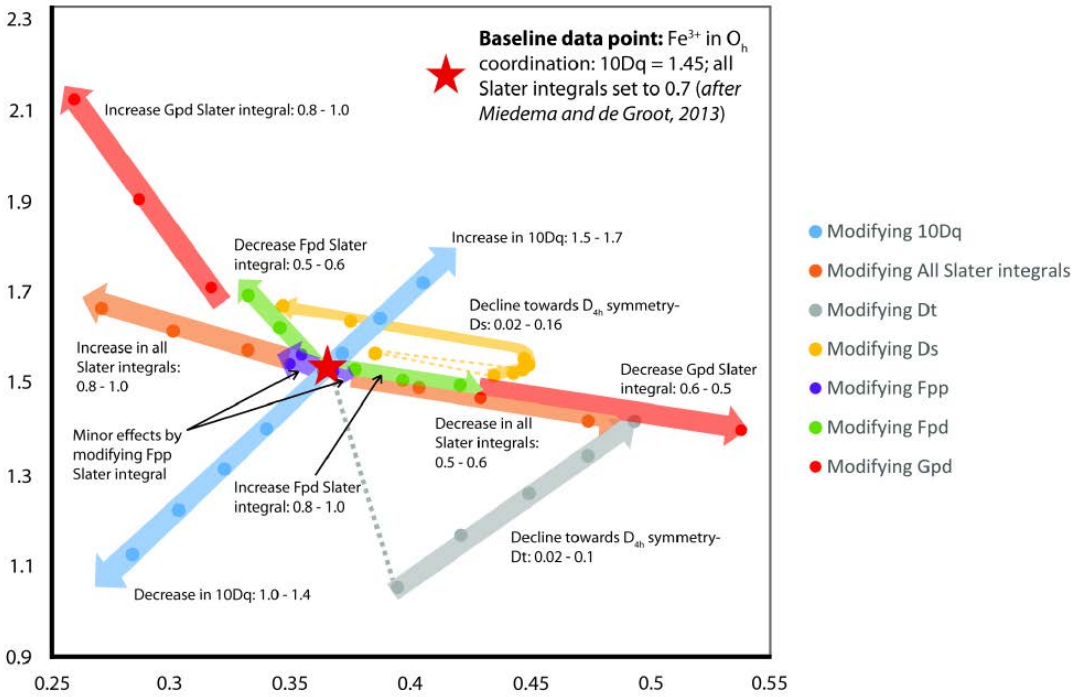

888
889

890 **Figure 3:**
891

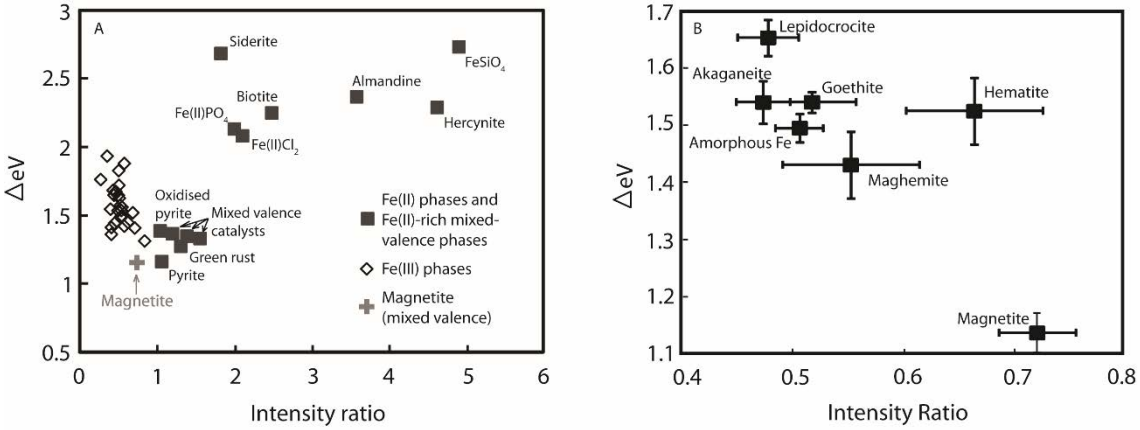

892
893
894

895 **Figure 4:**
896

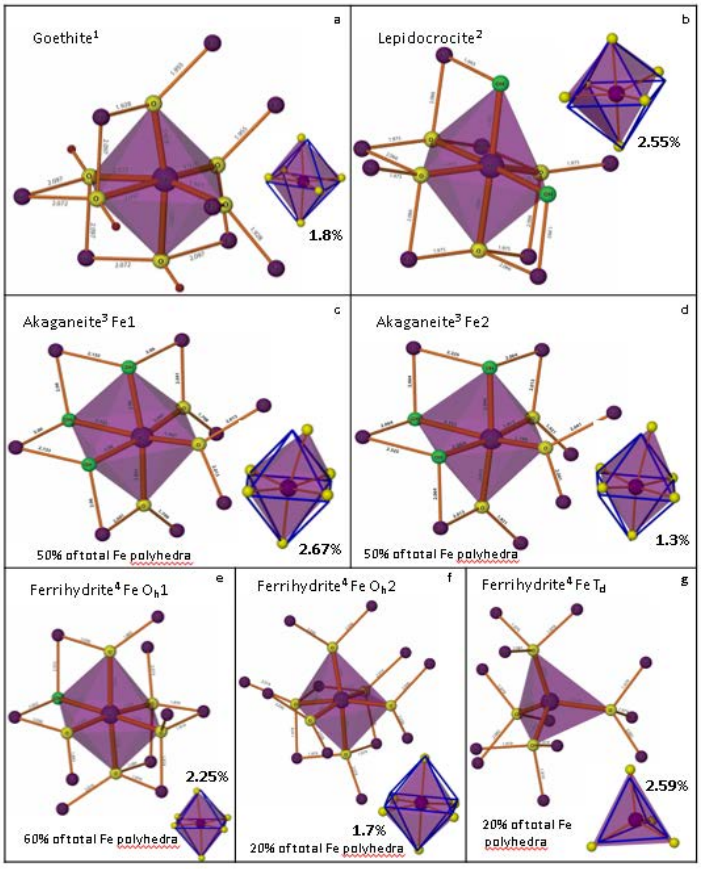

897
898

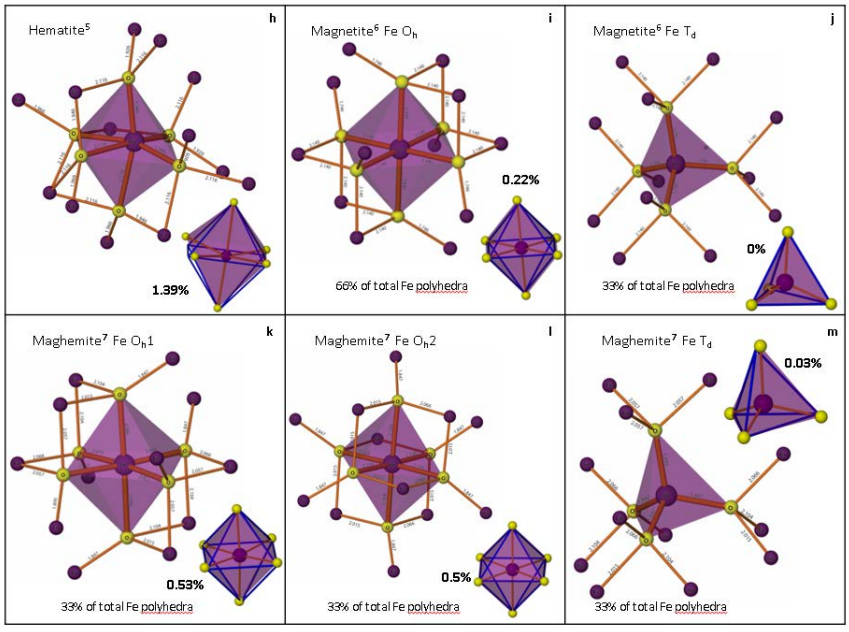

899

900

Figure 5:

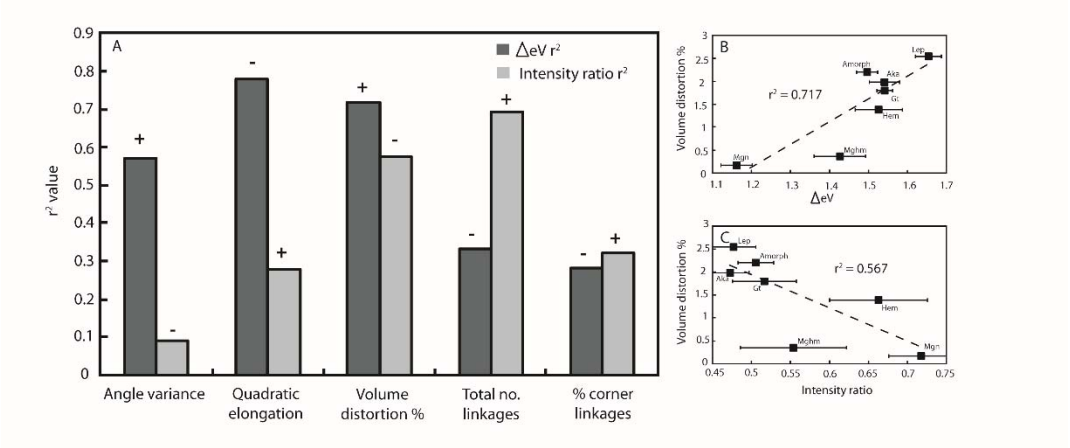

This is a preprint, the final version is subject to change, of the American Mineralogist (MSA)
Cite as Authors (Year) Title. American Mineralogist, in press.
(DOI will not work until issue is live.) DOI: http://dx.doi.org/10.2138/am-2017-5805

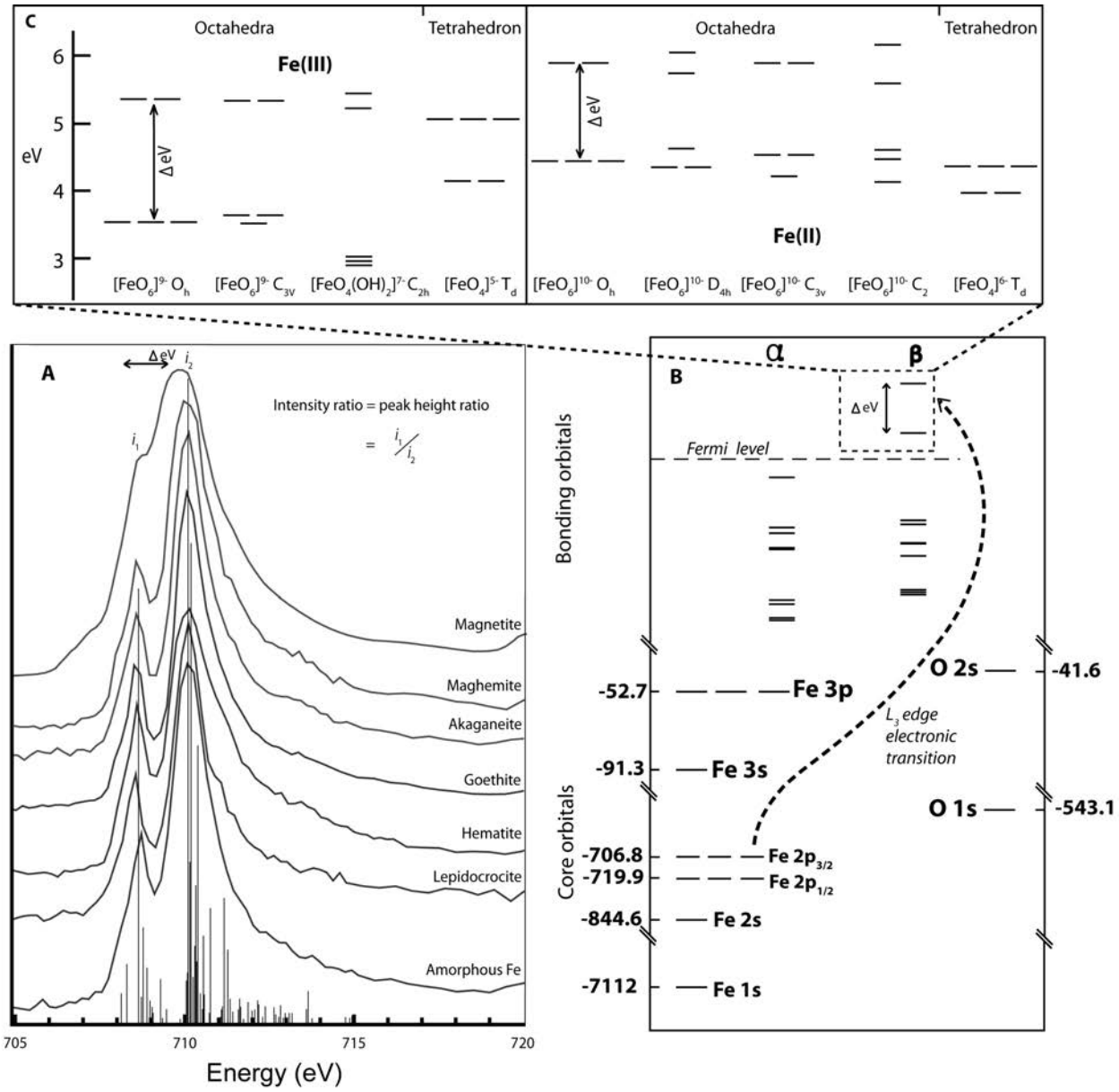

This is a preprint, the final version is subject to change, of the American Mineralogist (MSA)
Cite as Authors (Year) Title. American Mineralogist, in press.
(DOI will not work until issue is live.) DOI: http://dx.doi.org/10.2138/am-2017-5805

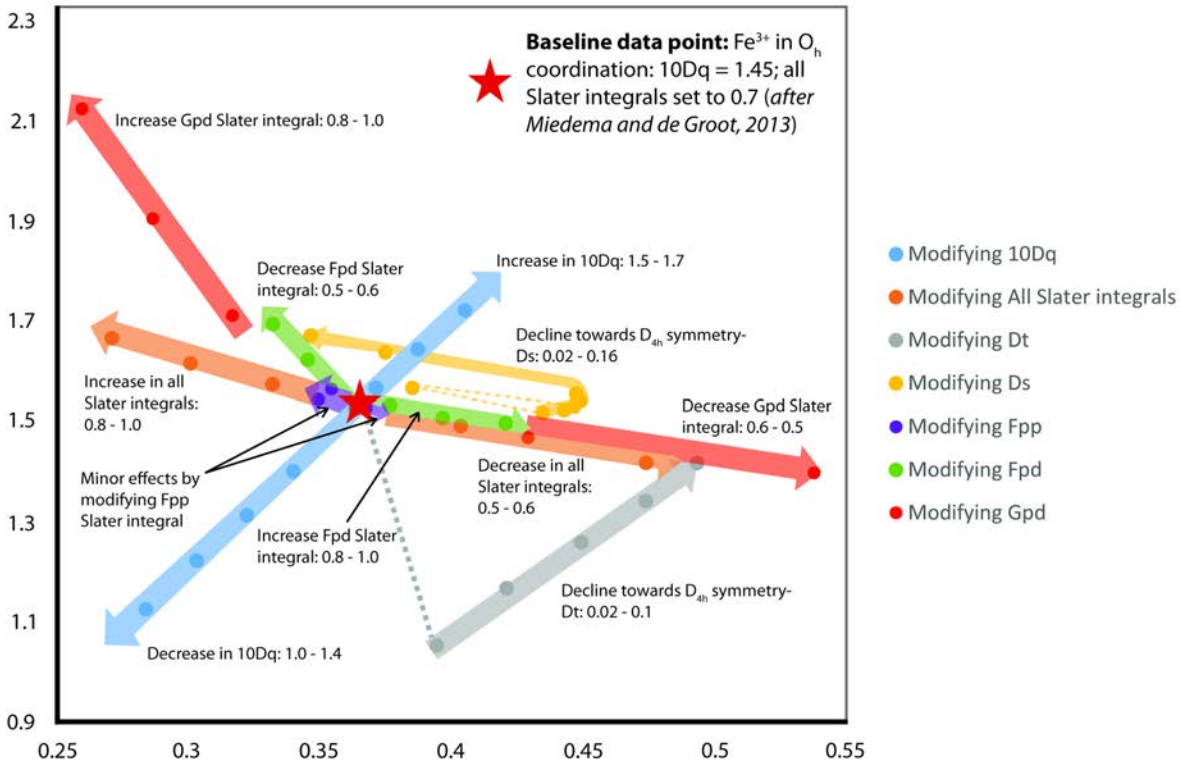

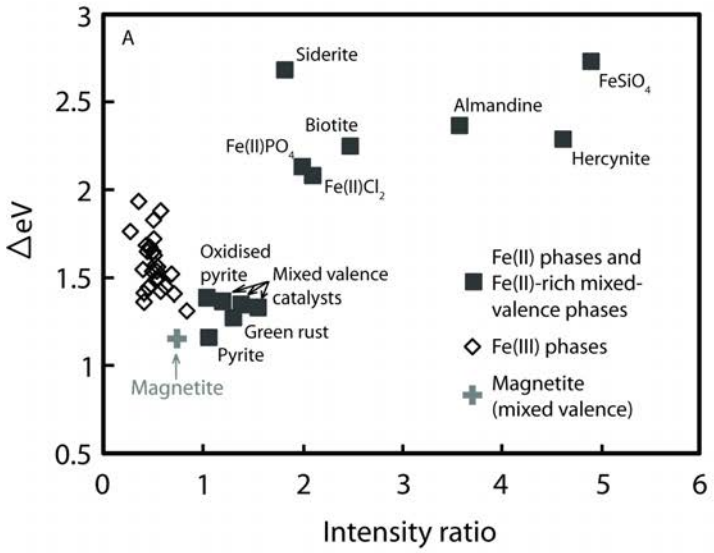
A
Siderite
FeSiO4
Almandine
Biotite
Fe(II)PO4
Hercynite
Fe(II)Cl2
Oxidised pyrite
Mixed valence catalysts
Green rust
Pyrite
Magnetite
Fe(II) phases and Fe(II)-rich mixed-valence phases
Fe(III) phases
Magnetite (mixed valence)
ΔeV
Intensity ratio

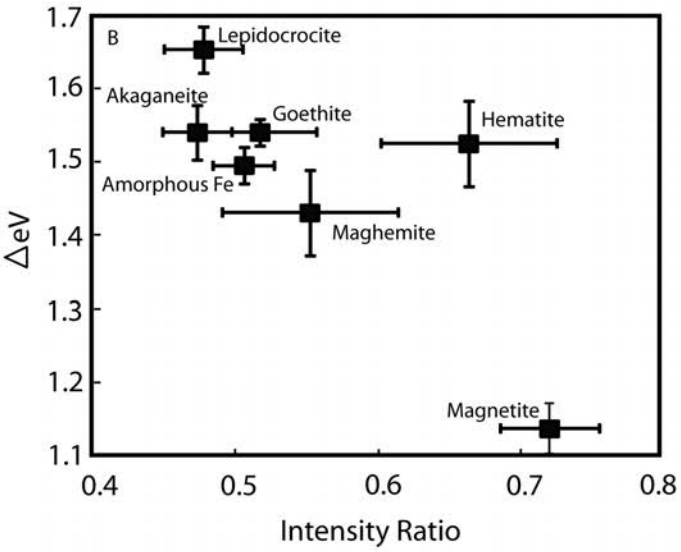
B
Lepidocrocite
Akaganeite
Goethite
Hematite
Amorphous Fe
Maghemite
Magnetite
ΔeV
Intensity Ratio

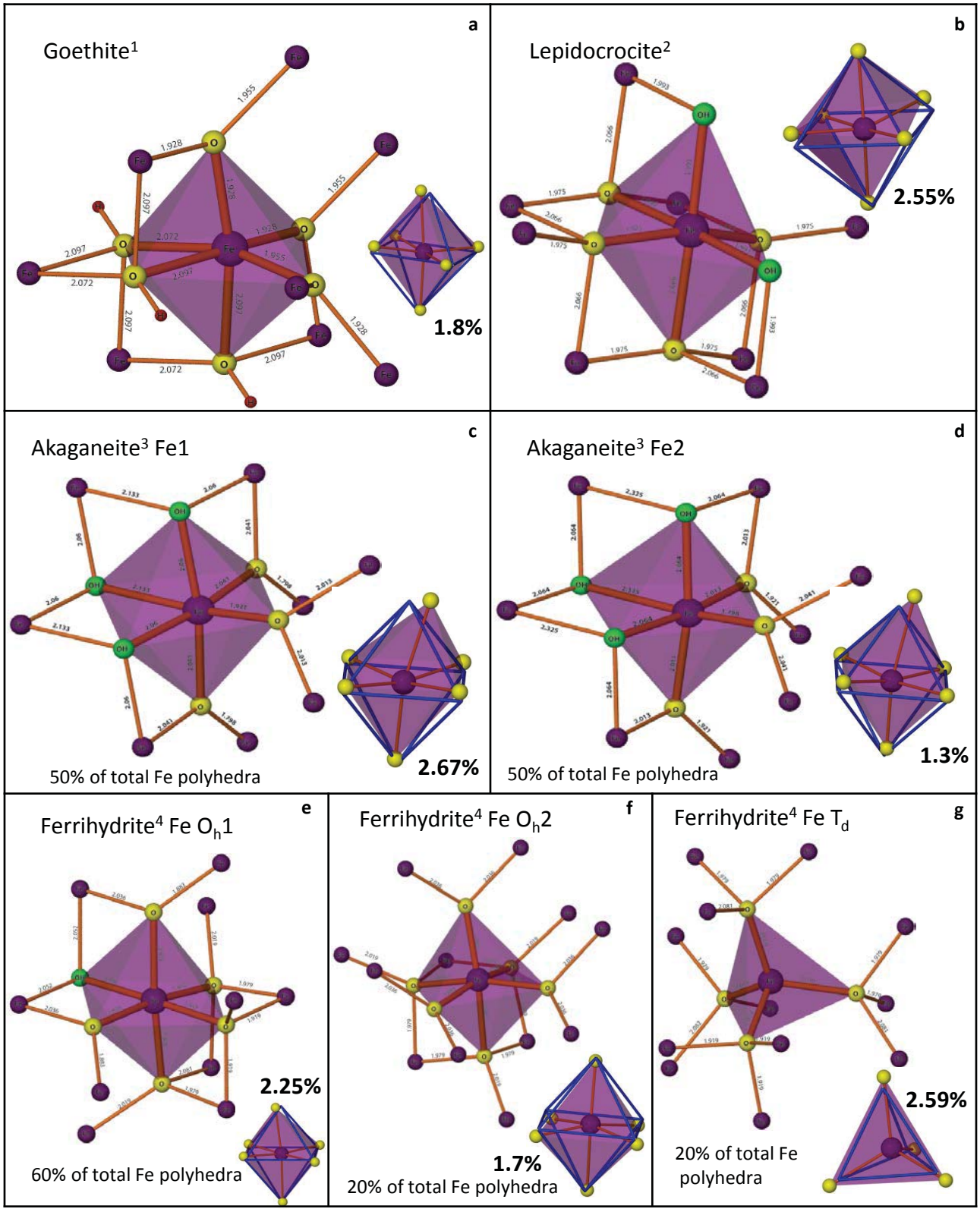

Fig. 3: *Iron polyhedra with local coordination for the Fe oxide and oxy-hydroxide mineral phases analyzed in this study. Polyhedral distortions are the result of chemical and mineralogical (i.e. number and type of polyhedral linkages) properties of the respective phases. Inset octahedra are relative to a perfect octahedron and give an idea of the bond angle distortions and volume distortion (% volume distortion measure indicated in bold). All bond lengths are in Angstrom units (Å) and all images were generated using XSeed (Atwood and Barbour, 2003) and crystallographic data from published references: [1]Gualtieri et al., 1999; [2]Wyckoff, 1963; [3]Post and Buchwald, 1991; [4]Michel et al., 2007; [5]Blake et al., 1966; [6]Fleet, 1986; [7]Shmakov et al., 1995.*

This is a preprint, the final version is subject to change, of the American Mineralogist (MSA)
Cite as Authors (Year) Title. American Mineralogist, in press.
(DOI will not work until issue is live.) DOI: http://dx.doi.org/10.2138/am-2017-5805

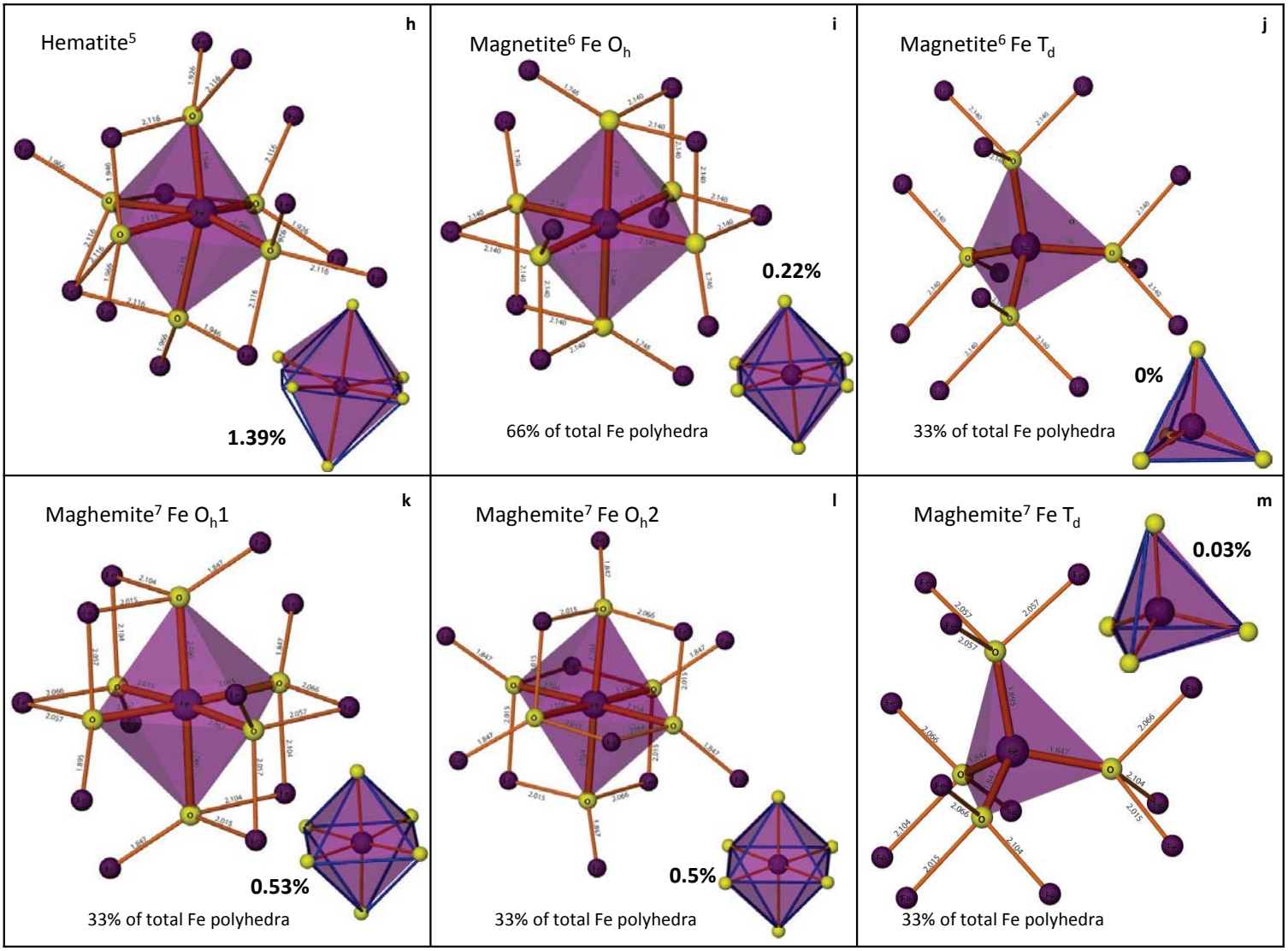

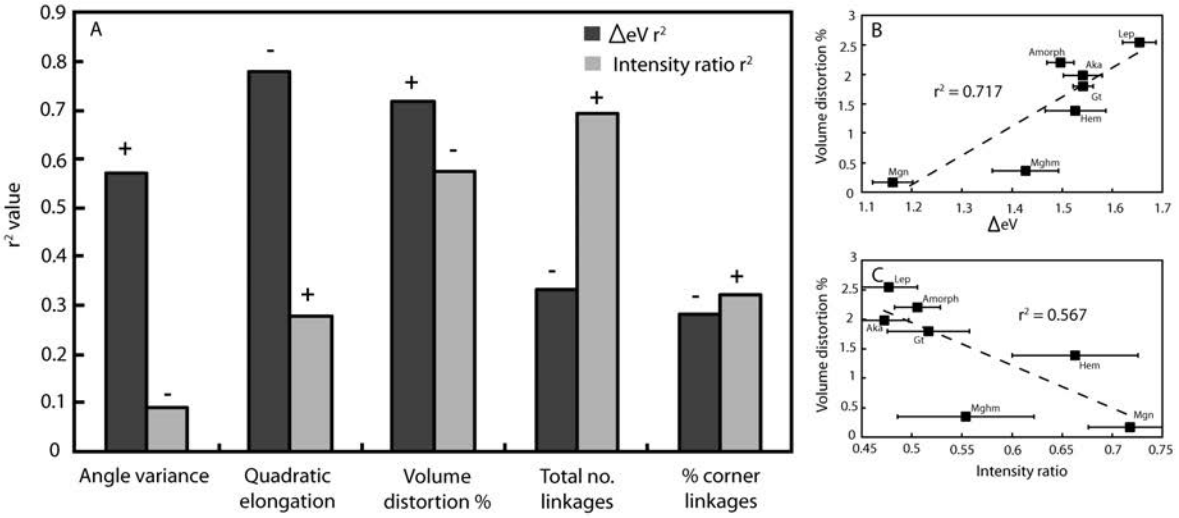
A
ΔeV r²
Intensity ratio r²
r² value
Angle variance
Quadratic elongation
Volume distortion %
Total no. linkages
% corner linkages
B
r² = 0.717
Volume distortion %
ΔeV
Lep
Amorph
Aka
Gt
Hem
Mgn
Mghm
C
r² = 0.567
Volume distortion %
Intensity ratio